Utilization of Landsat-8 Imagery and Aeromagnetic Data for Deciphering Alteration Zones and Structures: Implications for Mineral Exploration in the Southeastern Desert of Egypt

Ahmed Mohammed Eldosouky[a]*, Amin Beiranvand Pour[b], Abdelmgeed Hamed[a], Amira Taha[a], Mai Gamal[a], Ahmed Mahmoud[a], Luan Thanh Pham[c]

[a] Geology Department, Faculty of Science, Suez University, Suez, 43518, Egypt
[b] Institute of Oceanography and Environment (INOS), Universiti Malaysia Terengganu (UMT), 21030 Kuala Nerus, Terengganu, Malaysia
[c] Department of Geophysics, Faculty of Physics, University of Science, Vietnam National University, Hanoi, Vietnam.

ARTICLE INFO

ABSTRACT

Remote-sensing (RS) and aeromagnetic data implemented notable information for mineralization potentiality detection of ore deposits within Al-Allaqi region of the southeastern Desert of Egypt. Several approaches of remote-sensing and aeromagnetic data were implemented. Results of band ratios (BR) and Principal Component Analysis (PCA) practicing Landsat-8 successfully imaged the hydrothermally altered zones and the structures outlined by lithologic contacts, faults, and porphyry features (dyke-like structures). Lineaments well extracted using aeromagnetic datasets. CET system method was applied for generating a heat map of the structural complexity. Likewise, the CET Porphyry Analysis system was performed to extract the likely near-circular porphyry features that revealing a probable site of mineralization and to validate the remote sensing observations. Integrated outcomes showed that areas of highly complex structures, density (fractures/faults) are consistent with the detected hydrothermally altered areas that are rivaled with mining zones in Al-Allaqi region of the Southeastern Desert of Egypt. This approach can be broadly appropriate to other divisions of the Southeastern Desert of Egypt for mineral prospecting.

1. Introduction

Sensors onboard satellites and aircraft provide various data for analyzing surface and subsurface aspects of geological structures, lithologic assemblies and hydrothermally altered minerals. Identification of geological structures (e.g., faults and fractures) and mapping hydrothermally altered regions are indispensable for mineral exploring program (Sabins 1999; Pour and Hashim, 2012; Sheikhrahimi et al., 2019; Pour et al., 2018, 2019a,b,c,d; Sekandari et al., 2020a,b). Remote-sensing sensors allowed surface extracting the junctions and mapping hydrothermally altered zones (HAZ). These data highlight the contacts that are presumably placed along with structures (Ramsay and Huber, 1987; Hashim et al., 2013; Pour and Hashim, 2017). These structures could have exhibited a subsurface extension (Sabins, 1999).

Analysis and interpretation of aeromagnetic data allowed mapping the subsurface extension of geologic structures

_____

* Corresponding authors at: Suez University
E-mail addresses: dr_a.eldosoky@yahoo.com (A.M. Eldosouky)

(Abuelnaga et al., 2019; Eldosouky, 2019; Sehsah et al., 2019; Sehsah and Eldosouky, 2020; Eldosouky et al., 2020a,b,c; Pham et al., 2020c, 2021a,b,c; Eldosouky & Mohamed, 2021) and revealing porphyry intrusion (Gaafar, 2015; Holden et al., 2011; Wemegah et al., 2015; Eldosouky et al., 2020d). Aeromagnetic surveys play an essential role in searching for mineral deposits attributed to intrusions structures and shear zones. Mapping the structures by aeromagnetic data have significant roles in delineating the subsurface location of ore mineralizations (Elkhateeb & Eldosouky, 2016; Elkhateeb et al., 2018a,b; Assran et al., 2019). The function of aeromagnetic systems is procured from the anomalous responses caused by ferromagnetic mineralized zones. Integration of aeromagnetic, remote-sensing and geological data were applied to delineate the promising structural lineaments of ore mineralization in the eastern desert of Egypt (Gaafar, 2016; Eldosouky et al., 2017; El-Qassas et al. (2021) integrated aeromagnetic, remote-sensing, and geological data to delineate the promising structural sites of ore mineralization in the southeastern Desert of Egypt. The fusion of remote-sensing data and aeromagnetic systems,

as well as geological surveys, proved to be an applicable technique for deciphering the structural, geologic features, porphyry-features and HAZ associated with ore deposits. Aeromagnetic data can be utilized for detecting sub-surface fractures and faults that complement and validate the remote sensing analysis and interpretation. Accordingly, the present study aims at the integration of Landsat-8 satellite remote-sensing data and aeromagnetic data to delineate the HAZ as well as extracting the surface and sub-surface structures to highlight prospective zones of ore mineralization in Al-Allaqi region of the southeastern Desert (SED) of Egypt.

2. Geology of the Study area

The investigated region is a part of Al-Allaqi region in the Egyptian SED (Fig. 1). It extends from latitudes 22º 22'50"

to 23º 00'00"N and longitudes 33º 15' to 34º 15′ E. Based on the geological (EGSM 1996), the investigation area consisting of Neoproterozoic crystalline rocks, Cretaceous sandstone, Mesozoic, and younger volcanic and sub-volcanic rocks. The majority of the study area is formed from basement rocks but a small exhibition of sedimentary rocks covers the southwestern part. The basement rocks in this area containing the Ophiolitic group, Island-Arc Assemblage, and Granitoids (Fig. 1) (El-Nisr, 1997). The Granitoids are prevalent in the central part of the investigated region, especially close to Wadi Shelman (Fig. 1). They transpire as deeply-eroded, circular points with few separated low-lying cliffs draped by recent sand deposits.
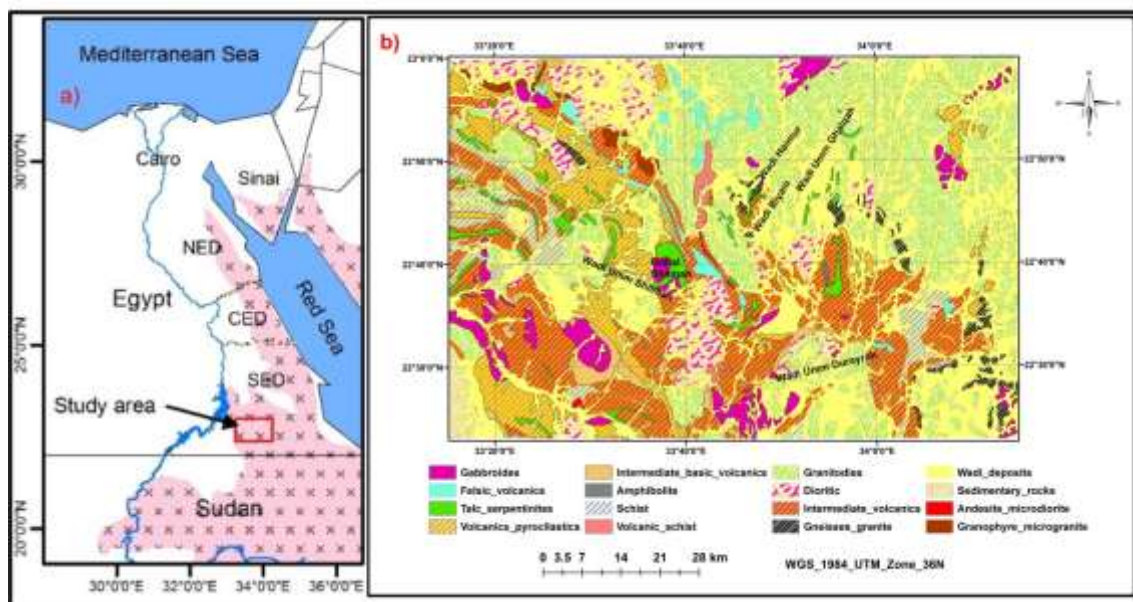

Figure 1. (a) Geoghraphical location; and (b) geology map of Al- Allaqi area (after Eldosouky et al, 2017).

3. Materials and methods

3.1. Remote-sensing data characteristics

Landsat-8 was begun on 4 February 2013 from Vandenberg Air Force Base in California. It is in the style of a free-flyer spaceship carrying two-sensors (the OLI and the TIRS). These two tools obtain data for nine visible, near-infrared, shortwave infrared bands and two long wave thermal bands. The OLI obtains spectral images in nine bands. The bands of OLI have a 30 m spatial resolution (15 m resolution for band 8). The TIRS assembles two thermal bands with 100 m spatial resolution. Landsat-8 images are gained in 185 km swaths and split into 185 × 180 km scenes suited for regional geologic investigation (Irons et al., 2012; Roy et al., 2014).

Landsat-8 images were captured through the U.S. Geological Survey EROS Center (http://earthexplorer.usgs.gov) was practiced in this study. The Landsat-8 image was processed utilizing the ENVI

version 5.3 software package. Landsat-8 data were transformed to surface reflectance using the Internal Average Relative Reflection (IARR) system (Ben-Dor et al., 1994). Ben-Dor et al. (1994) urged the IARR reflectance system for imaging minerals as a preferred calibration procedure, which does not necessitate preceding knowledge of samples gathered from the field. The panchromatic and cirrus cloud (band 9) bands, as well as TIR bands, have not been employed in this study.

3.2 Image processing techniques

The Band-ratioing (BR) approach is broadly employed for mapping HAZ of lithologic units. In this process, the digital number (DN) value of reflective and absorptive bands related to mineral or mineral groups is subdivided to each other. The bright pixels (high DN values pixels) successively appear in the rule image, which specifies the spectral features attributed to the particular mineral or mineral group that premeditated to identify (Tommaso and Rubinstein, 2007). Furthermore, this technique has a

proficiency for decreasing the topographic impacts produced from slope orientation and solar illumination angle (Colby, 1991). To discriminate iron oxide/hydroxides, the VNIR spectral bands comprise the most relevant data due to electronic transformations of Fe3+/Fe2+ in a VNIR spectrum from 0.45 to 1.2 µm (Clark, 1999). In this study for distinguishing an iron oxide, BR of 4/2 was elected to delineate iron oxide/hydroxides. Carbonates (calcite, gypsum, muscovite, kaolinite, and dolomite) and Hydroxyl-bearing (Al-OH) alteration display spectral absorption characteristics in 2.1–2.5 µm due to overtones and incorporations of the basic fluctuations (Hunt and Ashley, 1979), whereas their spectral reflectance occurs in 1.55–1.75 µm in the SWIR areas typically (Figure 4). These features are harmonized with bands 7 and 6(2.11–2.29, 1.57–1.65 µm) of Landsat-8. BR 6/5 was used to intensify the surface pattern of ferrous silicates.

The PCA is extensively employed to outline HAZ and lithologic assemblies employing spectral bands of RS sensors (Sheikhrahimi et al., 2019 and references therein). The uncorrelated lined aggregates (eigenvector loadings) bear significatory information allied to spectral features of altered minerals that can be presumed from the distinct spectral bands in the SWIR and VNIR regions (Crosta et al., 2003). Accordingly, a PC contains powerful eigenvector

loadings for characteristic bands (reflective and absorptive) of an altered mineral or mineral assemblage with opposing signs that enhance that mineral or mineral assemblage as light or dark pixels in the PC images. The positive charging in a reflective band intensifies the altered mineral as bright pixels, while negative loading is in a reflective band represents the altered mineral as dark ones (Crosta et al., 2003). In this analysis, the PCA system was performed based on covariance pattern to the decided bands 1 to 7 of Landsat-8. Table 1 presents the eigenvector matrix for elected bands.
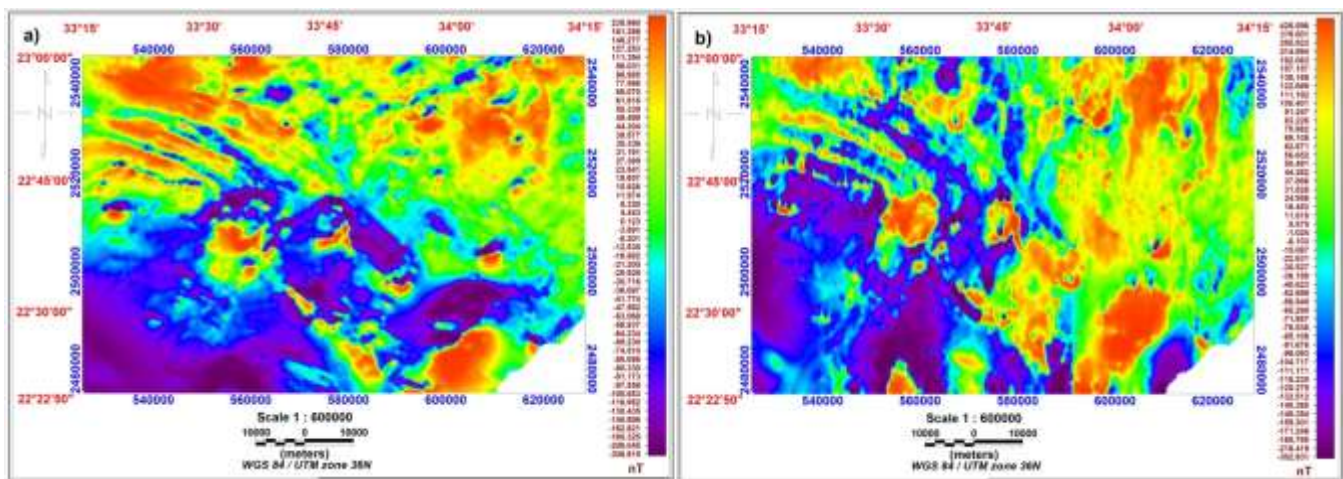
3.2 Aeromagnetic data

The Total Magnetic (TMI) data (Figure 2 a) were used in the present study (Aero-Service, 1984). Work the CET porphyry and grid operations lack reduction to the pole (RTP). Thus, the TMI map has improved and reduced to pole (RTP) (Baranov, 1957) after subtracting the theoretical IGRF (Figure 2 b).

The CET grid system improves the pattern of the magnetic data to outline complicated structural regions for exploring ore mineral deposits. The CET grid system is employed to recognize promising deposit zones.

Table 1. PCA statistical factors he selected bands 1 to 7 of Landsat-8.

	Band 1	Band 2	Band 3	Band 4	Band 5	Band 6	Band 7
PCA 1	0.08	0.10	0.24	-0.37	0.50	0.69	0.15
PCA 2	0.14	0.18	0.15	0.89	0.28	0.12	0.10
PCA 3	-0.35	**-0.62**	-0.30	**0.49**	0.11	0.08	-0.47
PCA 4	0.33	0.38	0.37	-0.18	**0.47**	**-0.50**	-0.29
PCA 5	-0.11	-0.21	-0.25	-0.09	0.32	**-0.48**	**0.57**
PCA 6	0.64	0.19	-0.72	-0.03	0.04	0.10	-0.13
PCA 7	0.08	-0.28	0.16	0.01	-0.01	0.00	-0.64

Figure 2. (a) Total Magnetic Intensity (TMI) and (b) Reduced to Pole (RTP) maps of Al-Allaqi area.

Previous knowledge of empirical connections between geologic characteristics and ore mineral deposits provides filtering the outcome. The CET system method recognizes the discontinuities in magnetization using a mixture of two-adjacent symmetric point delineation and texture analysis (Kovesi, 1997; Holden et al., 2010, 2011; Eldosouky et al., 2017,2020a). Subsequently, it analyzes domains of discontinuity and defines structural links to determine intersections, shifts, and junctions applying the next steps:

(i): Texture Enhancement – defines the regions of complicated textures connected to abrupt changes in magnetic values using the Standard Deviation (SD).

For a windowpane of N cells, whose essence value is μ, the SD σ of the cell values x_i is given by:

$$\sigma = \sqrt{\left[\frac{1}{N}\sum(x_i - \mu)^2\right]} \qquad (1)$$

The SD system provides a clearer image of the level of randomness that defeats the inherent noise in the grids.

(ii): Phase Symmetry (PS) – Implements the texture enhancement outcomes for recognizing regions of side discontinuity.

(iii): Structures Detection – Appropriates the effects of PS to decrease the discontinuities including areas into extended structures.

The CET porphyry system is applied to map the locations of the circular feature within data. The Central Peak Detection (CPD) plugin is then employed to determine the likely centers of the circular points (Holden et al., 2010).

4. Results and discussion

4.1 Remote sensing analysis

4.1.1 Band ratio results

Figure (3a) displays the RGB composite of 5 (0.85-0.88 μm), 2 (0.45-0.51 μm), and bands 7 (2.11-2.29 μm) of Landsat-8. Most of the lithological assemblages having different spectral peculiarities related to clay minerals, ferrous silicates, and iron oxide/hydroxides represent distinct colors. Reference to the geology map of Al-Allaqi area (see Figure 1), intermediate volcanics, intermediate-basic volcanics, granitoids, gabbroids, volcanic-schist, and dioritic units are appeared in brown to magenta color reflecting high content of ferrous silicates and iron oxide/hydroxides in their compositions. However, talc-serpentinites, volcanics-pyroclastics, wadi deposits are manifested as dark to light blue hues due to the different content of clay minerals. Sedimentary rock and some parts of wadi deposits are appeared in yellow shade, which can be attributed to the admixture of clay minerals and iron oxide/hydroxides. Figure (3b) shows an image-map of 6/7 band ratio that indicating alteration zones rich in hydrothermal clay minerals as bright pixels (high DN values). The spatial locations of chromite, Au, and Cu/Ni mines in the study area are overlaid on an image-map of the alteration zones (black pixels) derived from the 6/7
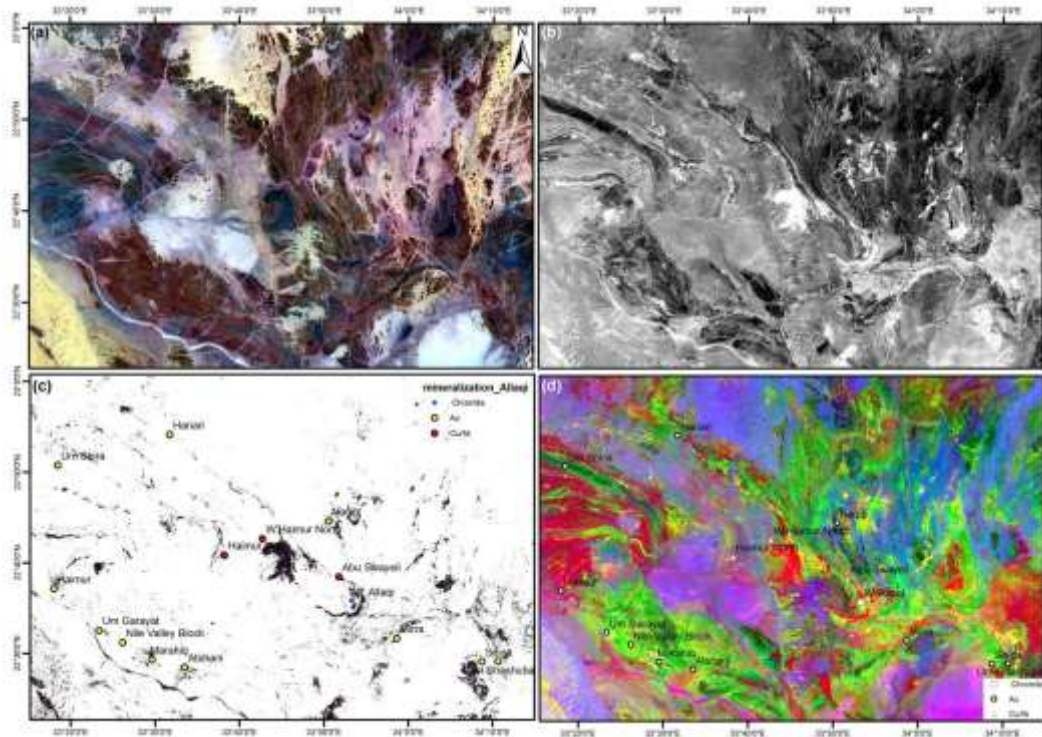
band ratio (Figure 3c). Most of the ore mineralization zones are located adjacent to the detected alteration area in Figure (3c). Au mining/mineralization zones are associated with intermediate volcanics and intermediate-basic volcanics background that are hydrothermally altered (Figure 3c). Chromite and Cu/Ni mining/mineralization zones are situated in gabbroidic background and associated with talc-serpentinites (Mg-OH alteration zone) (Figure 3c). Figure (3d) shows RGB composite of 6/7, 6/5, 4/2 band ratios. Lithological units are appropriately discriminated, and hydrothermal alteration zones are mapped as yellow colors that are associated with ore mineralization zones.
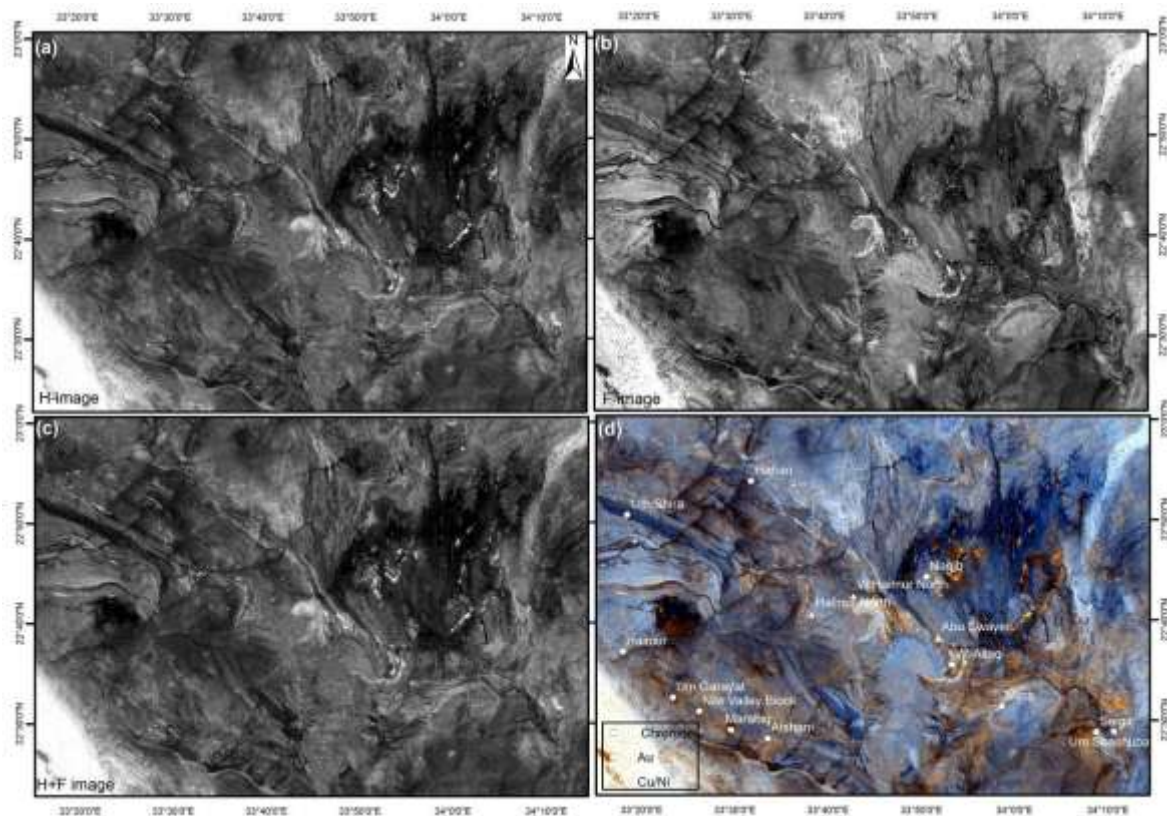
4.1.2 PCA results

The signs and amplitudes of the eigenvector loadings for PC3, PC4, and PC5 indicate that these PCs contain particular spectral information related to alteration minerals (Table 1). PC3 shows potent contributions of bands 2 (-0.62) and 4 (0.49) with opposing signs (Table 1). Iron oxide/hydroxide mineral assemblages exhibit potent absorption peculiarities in Landsat-8 band 2 (0.45-0.51 μm) and obvious reflection in Landsat-8 band 4 (0.64-0.67 μm) (Pour et al., 2018, 2019c) Therefore, the PC3 image enhance iron oxide/hydroxide minerals in as bright pixels (Figure 4 a). The PC4 eigenvector has notable loading of bands 5 (0.47) and 6 (-0.50) with opposite signs (Table 1). Ferrous silicates contain powerful absorption properties at 0.9–1.2 μm, which are equal to Landsat-8 bands 5 and 6 (Pour et al., 2019a,b). Hence, the PC4 image the surface abundance of ferrous silicates as bright pixels (Figure 4 b). PC5 has potent loadings of bands 6 (-0.48) and 7 (0.57) with opposed signs. Hydroxyl-bearing sulfate and clay groups and carbonates have a reflection in band 6 (1.57-1.65 μm) and absorption in band 7 (2.11-2.29 μm) of Landsat-8 (Pour et al., 2018). Consequently, the PC5 image shows the surface abundance of clays and carbonates as bright pixels (Figure 4 c). RGB color composite of the PC3, PC4 and PC5 images map the hydrothermal alteration zones as orange to a golden color in the investigated region (Figure 4d). Most of the known mineralization occurrences are associated with alteration zones (Figure 4d).
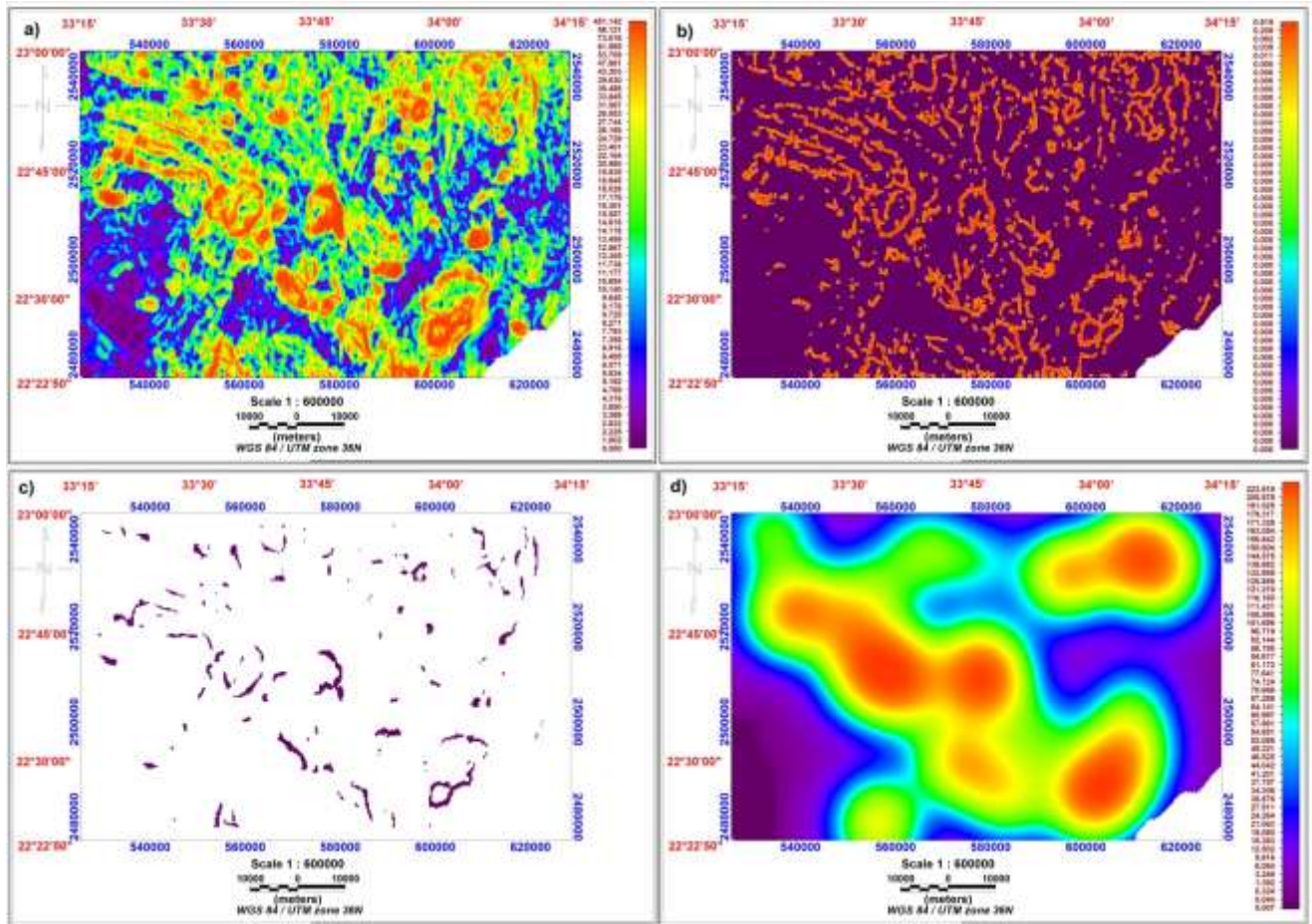
4.2 Aeromagnetic results

TMI map (see Figure 2a) shows broad differences in the values of magnetization varying from -308.815 to 235.960 nT. These values are either linked to lithological composition or the depths of the magnetic bodies. They are shown as variations in colors where the high (Orange) magnetic is related to mafic and ultramafic rocks and low magnetic (Purple) display the presence of metasediments and acidic rocks. TMI map (see Figure 2a) has long-wavelength and low gradient anomalies, weak responses over sediments at the southwestern part while display thin, elongated and more potent over the basements covering the eastern and northern parts of Al-Allaqi area. The RTP is applied to TMI data in figure 2a to reposition the anomalies directly over their source bodies (see Figure 2b).
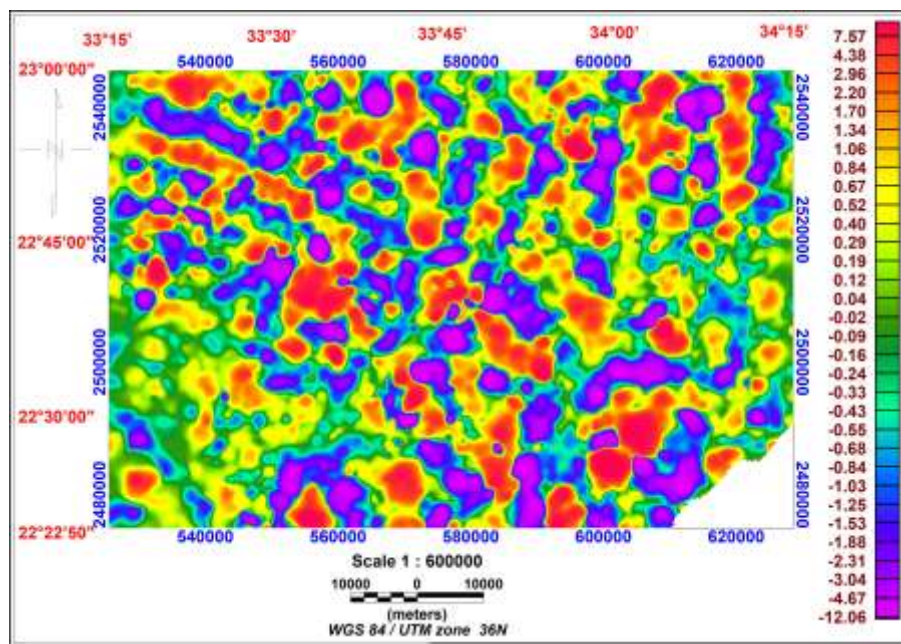
Figure 3. (a) RGB composite of bands 5, 2 and 7; (b) gray scale image map derived from 6/7 band ratio; (c) image-map of the alteration zones (black pixels) and spatial locations of chromite, Cu and Cu/Ni mines derived from 6/7 band ratio (d) RGB composite of 6/7, 6/5, 4/2 band ratios.

Figure 4. (a) PC3 image-map of Al-Allaqi area; (b) PC4 image-map of the study area; PC5 image-map of the study area; RGB color composite of the PC3, PC4 and PC5 images.

Figure 5. (a) Standard deviation (SD), (b) Phase symmetry (PS), (c) CET skeleton and (d) the lineament density maps of Al-Allaqi area.

Figure 6. CET porphyry system map of Al-Allaqi area.

The procedures of the CET grid system are employed to the RTP grid of the investigated territory. The SD is estimated to recognize the structurally complicated regions corresponded to discontinuities in magnetizations as a representation of texture analysis (Figure 5a). The PS utilizes the texture enhancement from the SD results for distinguishing zones of sidelong discontinuity (Figure 5b). The effects of PS are used to convert discontinuities zones into structures to produce the skeleton CET map (Figure 5c). Figure 5d shows the lineaments density extracted from the skeleton CET map.

Figures (5a-d) shows a significant multiple intersection zone with NW-SE trending. Each skeleton line in figure 5c reflects weak (shear) zones over this direction. The WNW, NW, NNE, and NE trends are the major structural directions. The investigation of the skeleton CET and lineament density maps (Figure 5c and 5d) represents that the high-density structures are arrayed along WNW, NW, and NE directions in the central and eastern parts associating basements and metasediments. The CET porphyry system is applied to the RTP grid of the investigation area to map dike-like structures (Figure 6). The CET porphyry system map (Figure 6) shows that the majority of circular features of the study area structurally controlled along the main directions delineated from the CET skeleton map.

The extracted lineaments from geologic and magnetic are shown in Figure (7a). The WNW, NNE, NW, NE and ENE are the main tectonic directions controlling the study area. The density of the magnetic structures is shown in Figure (7b). The alteration mineral zones were ranked according to their relative suitability for controlling the ore mineral deposits. A number of GIS layers, including fractures/faults, alteration zones, circular features, lineament map, CET grid, CET porphyry, BRs and PCA were combined using GIS spatial analyst technique in order to obtain the most area of mineralization. As a result, a mineral prospectivity map of Al-Allaqi area was generated (Figure 8).
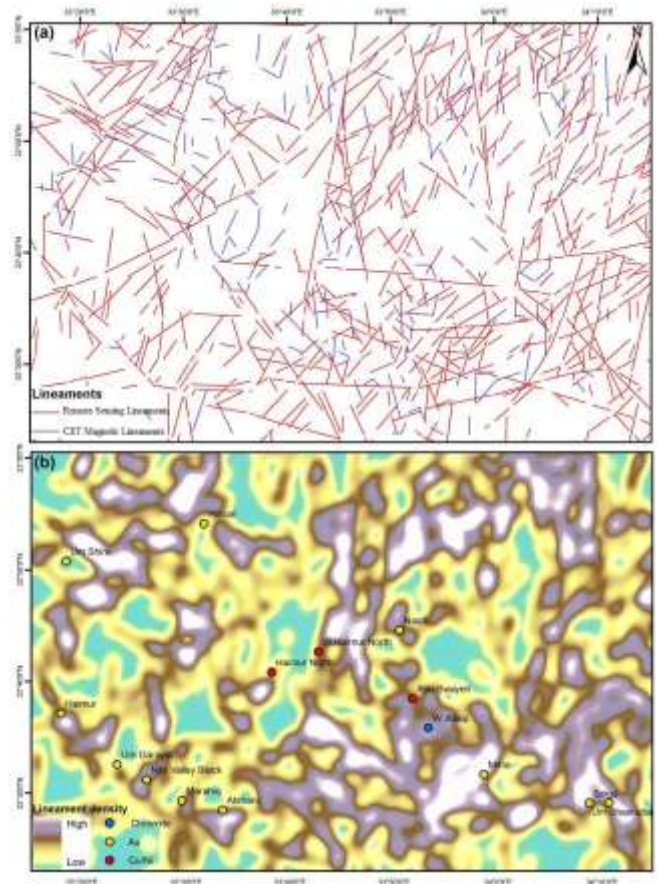
5. Conclusion

This investigation displays the employment of Landsat-8 remote-sensing and aeromagnetic data for delineating HAZ and structures to assist in mineral exploration at Al-Allaqi region of the SED of Egypt.

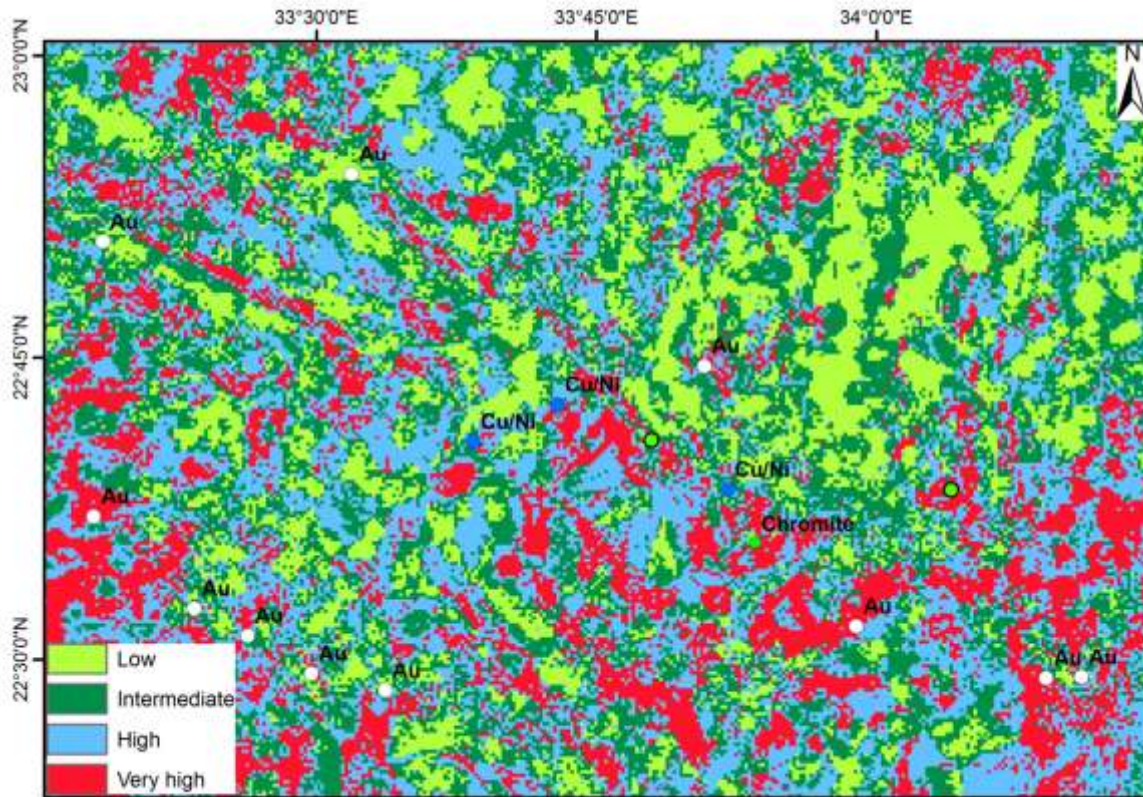Many HAZ of iron oxide/hydroxides, clays were distinguished practicing Landsat-8 remote-sensing data.

Aeromagnetic results showed that the WNW, NNE, NW, NE and ENE are the main tectonic trend controlling the ore minerals in the investigation area.

Integration of the outcomes clearly showed that the areas of high-density complex structures are consistent with the detected areas of hydrothermal alterations which are corresponding to mining zones in Al-Allaqi region of the SED of Egypt.

This approach can be extensively applicable to other parts of the ED of Egypt for mineral prospecting.

Figure 7. (a) Lineaments of the study area extracted from geologic and magnetic maps; (b) Lineament density map of Al-Allaqi area overlain by sites of mineralization.

Figure 8. Mineral prospectivity map of Al-Allaqi area.

References

Abuelnaga, H.S., Aboulela, H., El-Sawy, E.K., El Qassas, R.A.Y., (2019). Detection of structural setting that controlling Hammam Faroun area, using aeromagnetic and seismicity data, Gulf of Suez, Egypt. Journal of African Earth Sciences, Vol. 158, 103560. https://doi.org/10.1016/j.jafrearsci.2019.103560.

Aero-Service, (1984). Final operational report of airborne Magnetic / radiation Survey in the Eastern Desert, Egypt. Aeroservice for EGPC, Houston, Texas, April 1984. Six volumes. An internal report. No. 3609.

Assran, A.S.M., El Qassas, R.A.Y., Yousef, M. H. M., (2019). Detection of prospective areas for mineralization deposits using image analysis technique of aeromagnetic data around Marsa Alam-Idfu road, Eastern Desert, Egypt. Egyptian Journal of Petroleum, Vol. 28, Iss. 1, pp. 61-69. https://doi.org/10.1016/j.ejpe.2018.11.002.

Baranov, W. A., (1957). new method for interpretation of aeromagnetic maps: pseudo-gravimetric anoma-lies.Geophysics, 22(2): 359~383.

Ben-Dor, E., Kruse, F.A., Lefkoff, A.B., Banin, A., (1994). Comparison of three calibration techniques for utilization of GER 63-channel aircraft scanner data of Makhtesh Ramon, Nega, Israel. Photogrammetric Engineering and Remote Sensing, 60(11), 1339-1354.

Clark, R.N., (1999). Spectroscopy of rock and minerals and principles of spectroscopy. In: Rencz, A.N. (Ed.) Remote Sensing for the Earth Sciences: Manual of Remote Sensing 3. John Wiley Sons, New York, pp. 3–58.

Colby, J. D., (1991). Topographic normalization in rugged terrain. Photogrammetric Engineering and Remote Sensing, 57(5), 531–537.

Crosta, A.P., Souza Filho, C.R., Azevedo, F., Brodie, C., (2003). Targeting key alteration minerals in epithermal deposits in Patagonia, Argentina, Using ASTER imagery and principal component analysis. International Journal of Remote Sensing 24, 4233–4240.

Eldosouky, A.M., Abdelkareem, M., Elkhateeb, S.O., (2017). Integration of remote sensing and aeromagnetic data for mapping structural features and hydrothermal alteration zones in Wadi Allaqi area, South Eastern Desert of Egypt. J. Afr. Earth Sc. 130, 28–37.

Eldosouky, A. M., (2019). Aeromagnetic data for mapping geologic contacts at Samr El-Qaa area, North Eastern Desert, Egypt. Arab J Geosci (2019) 12: 2. https://doi.org/10.1007/s12517-018-4182-2.

Eldosouky, A.M., Pham, L.T., Hassan, P., Pradhan, M.B., (2020a). A comparative study of THG, AS, TA, Theta, TDX and LTHG techniques for improving source boundaries detection of magnetic data using synthetic models: A case study from G. Um Monqul, North Eastern Desert, Egypt. Journal of African Earth Sciences   170:103940. https://doi.org/10.1016/j.jafrearsci.2020.103940.

Eldosouky, A. M., Saada, A. S., (2020b). Source edge detection (SED) of aeromagnetic data: synthetic examples and a case study from Haimur area, south Eastern Desert, Egypt. Arabian Journal of Geosciences, 13:626. https://doi.org/10.1007/s12517-020-05653-8.

Eldosouky, A.M., Elkhateeb, S.O., Ali, A., Kharbish, S., (2020c). Enhancing linear features in aeromagnetic data using directional horizontal gradient at Wadi Haimur area, South Eastern Desert, Egypt. Carpathian J. Earth Environ. Sci. 15(2):323–326. https://doi.org/10.26471/ Cjees/2020/015/132.

Eldosouky, A. M., Sehsah, H., Elkhateeb, S. O., Pour, A. B., (2020d). Integrating aeromagnetic data and Landsat-8 imagery for detection of post-accretionary shear zones controlling hydrothermal alterations: The Allaqi-Heiani Suture zone, South Eastern Desert, Egypt. Advances in Space Research 65, 1008–1024. https://doi.org/10.1016/j.asr.2019.10.030.

Eldosouky, A. M., Mohamed, H., (2021). Edge detection of aeromagnetic data as effective tools for structural imaging at Shilman area, South Eastern Desert, Egypt. Arab J Geosci 14, 13. https://doi.org/10.1007/s12517-020-06251-4

Elkhateeb, S.O., Eldosouky, A.M., (2016). Detection of porphyry intrusions using analytic signal (AS), Euler Deconvolution, and Center for Exploration Targeting (CET) Technique Porphyry Analysis at Wadi Allaqi Area, South Eastern Desert, Egypt. Int. J. Sci. Eng. Res. 7 (6), 471–477. ISSN 2229-5518.

Elkhateeb, S. O., and Abdellatif, M. A. G., (2018a). Delineation potential gold mineralization zones in a part of Central Eastern Desert, Egypt using Airborne Magnetic and Radiometric data. NRIAG Journal of Astronomy and Geophysics (2018), https://doi.org/10.1016/j.nrjag.2018.05.010.

Elkhateeb, S.O., Eldosouky, A.M., Aboelabas, S., (2018b). Interpretation of Aeromagnetic Data to Delineate Structural Complexity Zones and Porphyry Intrusions at Samr El Qaa Area, North Eastern Desert, Egypt. International Journal of Novel Research in Civil Structural and Earth Sciences. Vol. 5, Issue 1, pp. 1–9.

El-Nisr, S.A., (1997). Late Precambrian volcanism at Wadi Allaqi, SE Desert, Egypt: evidence for continental arc/continetal margin environment. Journal of African Earth Sciences 24, 301–313.

El-Qassas, R.A.Y., Ahmed, S.B., Abd-ElSalam, H.F., Abu-Donia, A.M., (2021). Integrating of Remote Sensing and Airborne Magnetic Data to Outline the Geologic Structural Lineaments That Controlled Mineralization Deposits for the Area around Gabal El-Niteishat, Central Eastern Desert, Egypt. Geomaterials, Vol. 11, No. 1, pp. 1-21. https://doi.org/10.4236/gm.2021.111001.

Gaafar, I.M., (2015). Integration of geophysical and geological data for delimitation of mineralized zones in Um Naggat area, Central Eastern Desert, Egypt. NRIAG J. Astron. Geophys. 4, 86–99.

Gaafar, I.M., (2016). Geophysical Surveys for defining favorable structures for Uranium remobilization in Wadi Yoider, Southern Eastern Desert, Egypt. Egypt. Geophys. Soc., EGS J. 14 (1), 149–164.

Egyptian Geological Survey and Mining Authority (EGSMA), (1996). Geologic map of Wadi Jabjabah Quadrangle, Egypt, Scale 1:250000.

Gerovska, D., Stavrev, Y., and Arauzo-Bravo, M.J., (2005). Finite-difference Euler deconvolution algorithm applied to the interpretation of magnetic data from northern Bulgaria, Pure App. Geophys. 162, 591-608.

Gunn, P., (1997). Airborne Magnetic and Radiometric Survey. AGSO Journal of Australian Geology and Geophysics, 17,(2), 216p.

Hashim, M., Ahmad, S., Johari, M.A.M., Pour, A.B., (2013). Automatic lineament extraction in a heavily vegetated region using Landsat Enhanced Thematic Mapper (ETM+) imagery. Advances in Space Research 51, 874-890.

Holden, E.J., Kovesi, P., Dentith, M., Wedge, D., Wong, J.C., Fu, S.C., (2010). Detection of regions of structural complexity within aeromagnetic data using image analysis. In: Twenty Fifth International Conference of Image and Vision Computing New Zealand.

Holden,E.J., Fu, S.C., Kovesi,P., Dentith, M., Bourne, B., Hope, M., (2011). Automatic identification of responses from porphyry intrusive systems within magnetic data using image analysis. Journal of Applied Geophysics 74 (2011) 255–262.

Hunt, G.R.; Ashley, R.P., (1979). Spectra of altered rocks in the visible and near-infrared. Econ. Geol. 74, 1613–1629.

Irons, J.R., Dwyer, J.L., Barsi, J.A., (2012). The next Landsat satellite: The Landsat Data Continuity Mission. Remote Sensing of Environment 145, 154-172.

Kovesi, P., (1997). Symmetry and asymmetry from local phase. In: Proceedings of the Tenth Australian Joint Converenceon Artificial Intelligence, pp.2–4.

Pham, L.T., Eldosouky, A.M., Oksum, E.. Saada, S.A., (2020c). A new high resolution filter for source edge detection of potential data. Geocarto International. DOI: 10.1080/10106049.2020.1849414.

Pham, L. T., Oksum, E., Vu, M. D., Vo, Q. T., Le-Viet, K. D., Eldosouky. A. M., (2021a). An improved approach for detecting ridge locations to interpret the potential field data for more accurate structural mapping: A case study from Vredefort dome area (South Africa), Journal of African Earth Sciences 175: 104099.

Pham, L. T., Oksum, E., Nguyen, D. V., Eldosouky, A. M., (2021b). On the performance of phase-based filters for enhancing lateral boundaries of magnetic and gravity sources: a case study of the Seattle Uplift, Arabian Journal of Geosciences 14: 129.

Pham, L. T., Kafadar, O., Oksum, E., Eldosouky, A. M., (2021c). An improved approach for detecting the locations of the maxima in interpreting potential field data. Arabian Journal of Geosciences 14: 43.

Pour, A.M., Hashim, M., (2012). The application of ASTER remote sensing data to porphyry copper and epithermal gold deposits. Ore Geol. Rev, 44, 1–9.

Pour, A.B., Hashim, M., (2017). Application of Landsat-8 and ALOS-2 data for structural and landslide hazard mapping in Kelantan, Malaysia. Natural Hazards and Earth System Sciences. 17 (7):1285-1303.

Pour, A.B., Park, T.-Y., Park, Y., Hong, J., Zoheir, B., Pradhan, B., Ayoobi, I., Hashim, M., (2018). Application of Multi-Sensor Satellite Data for Exploration of Zn–Pb Sulfide Mineralization in the Franklinian Basin, North Greenland. Remote Sens. 10, 1186. https://doi.org/10.3390/rs10081186.

Pour, A.B., Hashim, M., Hong, J.K., Park, Y., (2019a). Lithological and alteration mineral mapping in poorly exposed lithologies using Landsat-8 and ASTER satellite data: north-eastern Graham Land, Antarctic Peninsula. Ore Geol. Rev. 108, 112–133. https://doi.org/10.1016/j.oregeorev.2017.07.018.

Pour, A.B., Park, Y., Crispini, L., Läufer, A., Hong, J.K., Park, T.-Y.S., Zoheir, B., Pradhan, B., Muslim, A.M., Hossain, M.S., Rahmani, O., (2019b). Mapping Listvenite Occurrences in the Damage Zones of Northern Victoria Land, Antarctica Using ASTER Satellite Remote Sensing Data. Remote Sens. 11, 1408. https://doi.org/10.3390/rs11121408.

Pour, A.B., Park, T.-Y., Park, Y., Hong, J.K., Muslim, A.M., Laufer, A., Crispini, L., Pradhan, B., Zoheir, B., Rahmani, O., Hashim, M., Hossain, M.S., (2019c). Landsat-8, Advanced Spaceborne Thermal Emission and Reflection Radiometer, and WorldView-3 Multispectral Satellite Imagery for Prospecting Copper-Gold Mineralization in the Northeastern Inglefield Mobile Belt (IMB). Northwest Greenland. Remote Sens.11, 2430. https://doi.org/10.3390/rs11202430.

Pour, A.B., Park, Y., Park, T.S., Hong, J.K., Hashim,M., Woo, J., Ayoobi, I., (2019d). Evaluation of ICA and CEM algorithms with Landsat-8/ASTER data for geological mapping in inaccessible regions. Geocarto Internatinal, 34, 785–816.

Ramsay, J.G., & Huber, M. I., (1987). The Techniques of Modern Structural Geology. Volume 2: Folds and Fractures. xi 391 pp. London, Orlando, San Diego, New York, Austin, Boston, Sydney, Tokyo, Toronto: Academic Press. Price UK £17.50 US $34.50 (paperback). ISBN 0 12 576902 4 (hard covers); 0 12 576922 9 (paperback). Geological Magazine, 125(3), 316-317. doi:10.1017/S0016756800010384

Roy, D.P., Wulder, M.A., Loveland, T.A., Woodcock, C.E., Allen, R.G., Anderson, M.C., (2014). Landsat-8: Science and product vision for terrestrial global change research. Remote Sensing of Environment 145, 154-172.

Sabins, F.F., (1999). Remote sensingfor mineral exploration. Ore Geology Reviews, 14, 157–183. doi:10.1016/S0169-1368(99)00007-4

Sehsah, H., Eldosouky, A. M., and El Afandy, A. H., (2019). Unpaired ophiolite belts in the Neoproterozoic Allaqi-Heiani Suture, the Arabian-Nubian Shield: Evidences from magnetic data. Journal of African Earth Sciences 156 (2019) 26–34. https://doi.org/10.1016/j.jafrearsci.2019.05.002.

Sehsah, H., & Eldosouky, A.M., (2020). Neoproterozoic hybrid forearc – MOR ophiolite belts in the northern Arabian-Nubian Shield: no evidence for back-arc tectonic setting, International Geology Review, DOI: 10.1080/00206814.2020.1836523.

Sekandari, M., Masoumi, I., Pour, A.B., Muslim, A.M., Rahmani, O., Hashim, M., Zoheir, B., Pradhan, B., Misra, A., Aminpour, S.M., (2020a). Application of Landsat-8, Sentinel-2, ASTER and WorldView-3 Spectral Imagery for Exploration of Carbonate-Hosted Pb-Zn Deposits in the Central Iranian Terrane (CIT). Remote Sens. 12, 1239.

Sekandari, M., Masoumi, I., Pour, A.B., Muslim, A.M., Hossain, M.S., Misra, A., (2020b). ASTER and WorldView-3 satellite data for mapping lithology and alteration minerals associated with Pb-Zn mineralization. Geocarto Int. 1–23.

Sheikhrahimi, A., Pour, A.B., Pradhan, B., Zoheir, B., (2019). Mapping hydrothermal alteration zones and lineaments associated with orogenic gold mineralization using ASTER data: A case study from the Sanandaj-Sirjan Zone, Iran. Adv. Space Res. 63, 3315–3332.

Tommaso, D.I., Rubinstein, N., (2007). Hydrothermal alteration mapping using ASTER data in the Infiernillo porphyry deposit, Argentina. Ore Geology Reviews, 32, 275-290.

Wemegah, D.D., Preko, K., Noye, R.M., Boadi, B., Menyeh, A., Danuor, S.K., Amenyoh, T., (2015). Geophysical Interpretation of Possible Gold Mineralization Zones in Kyerano, South-Western Ghana Using Aeromagnetic and Radiometric Datasets. J. Geosci. Environ. Protection 3, 67–82. https://doi.org/10.4236/gep.2015.34008.